Experimental study of precessing instabilities in the cold flow field of a sudden expansion dump combustor

T. Holemans[1], Z. Yang[1], S. Van den Bosch[2], J. De Greef[3] , M. Vanierschot[1,*]

1: Department of Mechanical Engineering, Group T Leuven Campus, KU Leuven, Belgium
2: Sustainable Catalysis and Engineering, KU Leuven, Belgium
3: Sustainable Materials Processing and Recycling, Group T Leuven campus, KU Leuven, Belgium
*Corresponding author: maarten.vanierschot@kuleuven.be

Keywords: Sudden Expansion Flows, Precessing Instabilities, Spectral Proper Orthogonal Decomposition, Stereoscopic Particle Image Velocimetry

ABSTRACT

Stereoscopic Particle Image Velocimetry (SPIV) measurements are performed to analyse the cold flow field in a sudden expansion dump combustor geometry, with an expansion ratio of 4.9. The Reynolds number is varied from 5200 till 63300. The time-averaged flow field is found to be axisymmetric and has a jet-like velocity profile near the nozzle with a spreading rate comparable to free round jets. Despite the axisymmetric nature of the mean flow field, it contains unsteady coherent structures, which are analysed using the Spectral Proper Orthogonal Decomposition (SPOD) method. It is found that the instantaneous flow field is asymmetric and it precesses around the central axis of the geometry. The structure of this precession is similar for all Reynolds numbers investigated and the Strouhal number increases with increasing Reynolds number till a value of 26000, after which it reaches a constant value of around 3×10^{-3}. These precessing structures were previously only reported for swirling sudden expansion flows, where they are extensively studied, but this study shows they also exist in the non-swirling flow case.

1. Introduction

Sudden expansion flows can be found in a wide range of engineering applications such as heat exchangers, chemical reactors, cyclone separators, etc. Sudden expansion flows have been extensively studied, mostly for two-phase and/or swirling flows (Ahmed et al., 2008; Dellenback et al., 1988; Durrett et al., 1988; Vanierschot & Van den Bulck, 2008; Wang et al., 2004). Many of these researches focus on the reattachment length for specific boundary conditions and not as much on the temporal characteristics of the flow. Dellenback et al. (1988) measured different Reynolds numbers (30.000 to 100.000) and a range of swirl numbers from zero till 1.2. Both the time averaged flow fields and the temporal behavior were reported. For the zero-swirl case, no specific frequency could be identified in the spectra and hence the general structure of the flow was assumed to be steady, while for the swirling flow fields, a clear precession could be identified. These results are

also confirmed in the URANS simulations by Guo et al. (2001). They stated that a steady structured flow field is present up to a swirl number of 0.044. A study by Wang et al. (2004) performed Laser Doppler Velocimetry measurements and Large Eddy Simulations of a confined (swirling) flow in a sudden expansion. They also found no low frequency oscillation for the non-swirling case.
To the authors' knowledge, a detailed analysis of non-swirling sudden expansion flows using Stereoscopic Particle Image Velocimetry (SPIV) is currently lacking. This study aims to fill this gap by performing SPIV measurements for Reynolds numbers between 5200 and 63300. The mean velocity fields and profiles are analysed and low frequency instabilities are identified using Spectral Proper Orthogonal Decomposition (SPOD). The dependency of the dominant frequency and the shape of the spatial instabilities on the Reynolds number is also investigated.

2. Experimental setup and data processing

2.1. Experimental setup

A view of the experimental setup is shown in Figure 1. The geometry is a sudden expansion dump combustor with a nozzle based on the work of Vanierschot (2007). The modification made to this nozzle is the removal of the annular tube and hence introducing a pipe flow instead of an annular flow. The diameter of the inlet tube is $D_0 = 22.5$ mm and the one of the vessel $D_v = 110$ mm, giving an expansion ratio D_v/D_0 of 4.9. Water is used as medium and a frequency controlled pump (Packo NP/68-50/152) drives the flow. The flow rate is adjusted by a valve downstream of the reactor, giving a range of Reynolds numbers between 5200 and 63300 based on the mean velocity and diameter of the inlet tube, as shown in Table 1. The cylinder and octogonal confinement are both made of transparent PMMA. The volume between confinement and cylinder is filled with water to minimise refraction issues.

Table 1. Measured Reynolds numbers and their associated errors

	Reynolds number [-]
Measurement 1	5200 $\pm$75
Measurement 2	13500 $\pm$290
Measurement 3	25300 $\pm$715
Measurement 4	38400 $\pm$1990
Measurement 5	50500 $\pm$2615
Measurement 6	63300 $\pm$4065

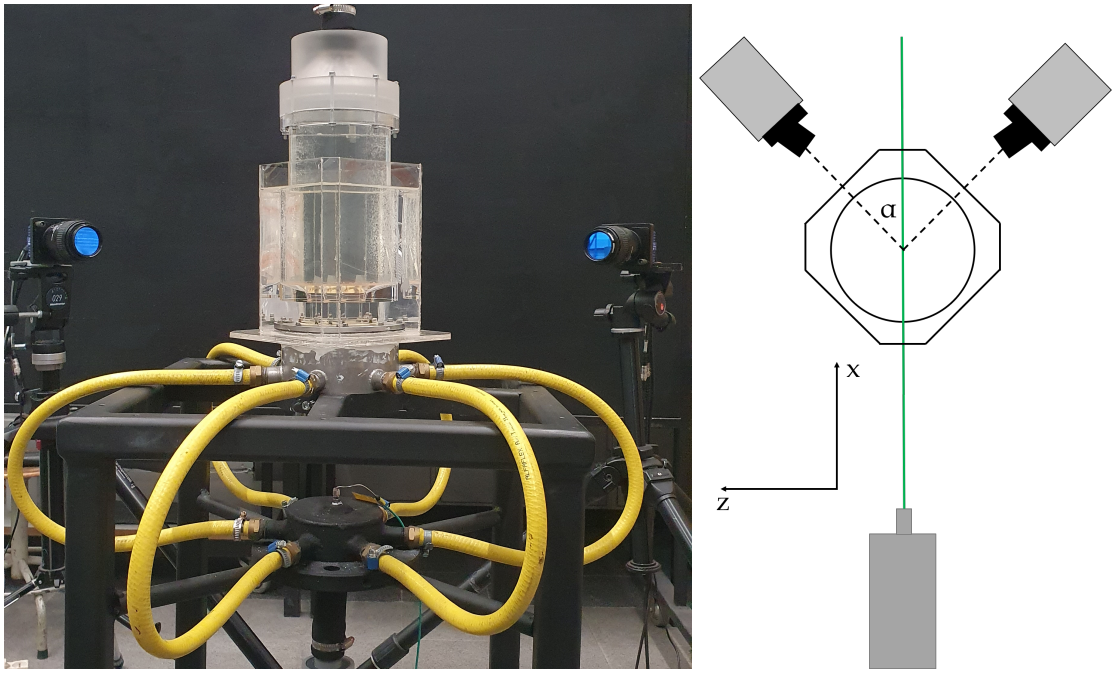

Figure 1. Left: photograph of the cameras and setup, viewed from a laser perspective. Right: topview of the SPIV setup with laser, setup, confinement and cameras shown

2.2. Stereoscopic particle image velocimetry

The velocity field is measured using SPIV measurements. A schematic representation of the SPIV configuration is shown in the right of Figure 1. The laser sheet contains the central axis of the geometry, measuring the velocity field in a median plane (xy-plane). The laser sheet has a thickness of 1mm. At angles α of 51.5° and 52.7° for both cameras respectively, they are looking at the measurement plane in a forward scattering position. A Scheimplug corrector ensures focusing of the entire measurement area. The seeding particles are hollow PMMA particles with a diameter of 20-50 μm, coated with Rhodamine B for fluorescence. These fluorescent particles allow higher laser intensities and more qualitative pictures, since wall reflections can be filtered out using a bandpass filter. The laser used is a Dual Cavity Nd:YAG PIV-laser from Litron with a wavelength of 532nm and a pulse energy of 200mJ. The pulse frequency of the laser is 12.95Hz, which results in a maximum measurable frequency of 6.47Hz, according to the Nyquist–Shannon sampling theorem. The two cameras are Imager SX6M cameras, which have a resolution of 2752×2200 pixels. The camera lens on both cameras is a AF Micro-Nikkor 60mm f/2.8D. The calibration of the cameras is done with a 3D calibration plate to correct for refraction. This calibration results in a total measurement domain of 105.3 mm by 100.73 mm, i.e. 2208×2112 pixels. The processing of the captured images to vector fields is done using Davis 10.2. The vector calculation takes place in multiple processing steps where the first interrogation area size is 96×96 pixels and the final one is 48×48 pixels, with an overlap of 50%. This gives a spatial resolution of 1.14mm between adjacent vectors. Two criteria are used to delete possible erroneous vectors: any vector with a correlation value lower than 0.5 is removed and a 4-pass regional median filter checks the correlation map for the second and third

highest peak and if these are less than 4 standard deviations different to the neighbouring vectors average, they are used. These two post-processing steps are applied to the final vector field and remaining missing vectors are interpolated from their neighbours.

2.3. Spectral Proper Orthogonal Decomposition (SPOD)

To capture the relevant flow dynamics of the jet flow, we apply snapshot SPOD as reduced order modelling technique (Sieber et al., 2016). Snapshot SPOD has already shown its capabilities for both swirling and non-swirling jet flows (Rovira et al., 2021; Vanierschot et al., 2020, 2021; Zhang & Vanierschot, 2021). The velocity field is decomposed into a mean and fluctuating part:

$$\boldsymbol{V}(\boldsymbol{x},t) = \overline{\boldsymbol{V}}(\boldsymbol{x}) + \boldsymbol{V}^{\dagger}(\boldsymbol{x},t) = \overline{\boldsymbol{V}}(\boldsymbol{x}) + \sum_{i=1}^{N} \boldsymbol{a}_i(t)\boldsymbol{\Phi}_i(\boldsymbol{x}). \tag{1}$$

In this equation, the fluctuating part is written as a set of spatial modes $\boldsymbol{\Phi}_i(\boldsymbol{x})$ and temporal coefficients $\boldsymbol{a}_i(t)$. $\boldsymbol{V}$ is a velocity vector with components u, v and w and the overbar denotes time averaged quantities. The temporal coefficients $\boldsymbol{a}_i = [a_i(t_1),\, a_i(t_2), ..., a_i(t_N)]^T$ and mode energies λ_i can be obtained by solving the eigenvalue problem,

$$\boldsymbol{R}\boldsymbol{a}_i = \lambda_i \boldsymbol{a}_i; \;\; \lambda_1 \geq \lambda_2 \geq \cdots \geq \lambda_n \geq 0, \tag{2}$$

where the elements of the correlation matrix $\boldsymbol{R}$ are given by

$$R_{i,j} = \frac{1}{N} \left\langle \boldsymbol{V}^{\dagger}(\boldsymbol{x},t_i), \boldsymbol{V}^{\dagger}(\boldsymbol{x},t_j) \right\rangle. \tag{3}$$

The spatial modes are obtained by the projection of the fluctuating velocity fields onto the temporal coefficients as

$$\boldsymbol{\Phi}_i(\boldsymbol{x}) = \frac{1}{N\lambda_i} \sum_{j=1}^{N} \boldsymbol{a}_i(t_j)\boldsymbol{V}^{\dagger}(\boldsymbol{x},t_j). \tag{4}$$

If periodic coherent structures exist in the flow field, the matrix $\boldsymbol{R}$ has a diagonal wave-like structure, also named diagonal similarity (Sieber et al., 2016). In SPOD, this similarity is augmented by filtering the correlation matrix $\boldsymbol{R}$ along the diagonals using a simple low-pass filter. This introduces the correlation matrix $\boldsymbol{S}$, defined as

$$S_{i,j} = \sum_{k=-N_f}^{N_f} g_k R_{i+k,j+k}, \tag{5}$$

with $\boldsymbol{g}$ a vector of length $2N_f$+1 with filter coefficients and N_f the filter width. The correlation matrix $\boldsymbol{S}$ can be substituted $\boldsymbol{R}$ in Equation 2 and the velocity field is decomposed using $\boldsymbol{S}$ instead

of $\boldsymbol{R}$. The optimal filter width was shown to be in the order of one or two times the period of the coherent structure of interest if it is pronounceable present (Sieber et al., 2016) or 4 to 8 times if intermittently present (Vanierschot et al., 2020). In this study, a filter width of 1.5 times the period is chosen as the structures are notable present.

3. Results

3.1. Accuracy of PIV measurements

The errors involved in SPIV measurements can be divided in systematic errors and random errors (ITTC, 2014; Sciacchitano, 2019). The major systematic errors are misalignment of the PIV setup and tracing accuracy of the seeding particles. The former are kept as small as possible by careful alignment of the laser sheet and the calibration plate. Calibration of the two cameras gives an RMS fit error of 0.86 and 1.75 pixels for each camera respectively. Analysing coherent 3D structures based on 2D PIV-measurements with SPOD introduces a maximum deviation of 10% due to the decrease of data, according to Holemans et al. (2022). To ensure accurate flow tracing, the Stokes number of the largest particle diameter (50 μm),

$$Sto = \frac{\tau_P}{\tau_f}, \tag{6}$$

is 0.021. An acceptable flow tracing accuracy is achieved when the Stokes number is below 0.1 (Raffel et al., 2018). As characteristic time scale of the flow, τ_f, the ratio of the nozzle diameter and axial velocity of the jet is taken. τ_P is given by following formula:

$$\tau_P = \frac{\rho_p d_p^2}{18\mu}. \tag{7}$$

The major random error is the peak estimation error. This error in combination with the sampling error decreases for the mean and RMSE velocity fields with an increasing number of effective samples according to equation 8,

$$\delta_{\overline{U_i}} = \frac{Z_{\alpha/2}}{\sqrt{N}} \frac{\sqrt{\overline{u_i u_i}}}{\overline{U_i}} \text{and} \qquad \delta_{\sqrt{\overline{u_i u_i}}} = \frac{\mathrm{Z}_{\alpha/2}}{\sqrt{2\mathrm{N}}}, \tag{8}$$

where $\overline{U_i}$ is the time-averaged velocity component i and $\sqrt{\overline{u_i u_i}}$ the associated RMSE value. The number of samples N is 3000 for each SPIV measurement. Representative profiles of $\overline{U_i}$ and $\sqrt{\overline{u_i u_i}}$ with error bars are plotted at $Y/D_0 = 0.5$ in Figure 2.

3.2. Time-averaged flow fields

The time-averaged and RMSE axial velocity fields at Re=38400 are shown in Figure 3. The other measured Reynolds numbers show a similar shape and distribution and hence the figure is representative for all measurements. Close to the combustor inlet, the velocity profile resembles a jet.

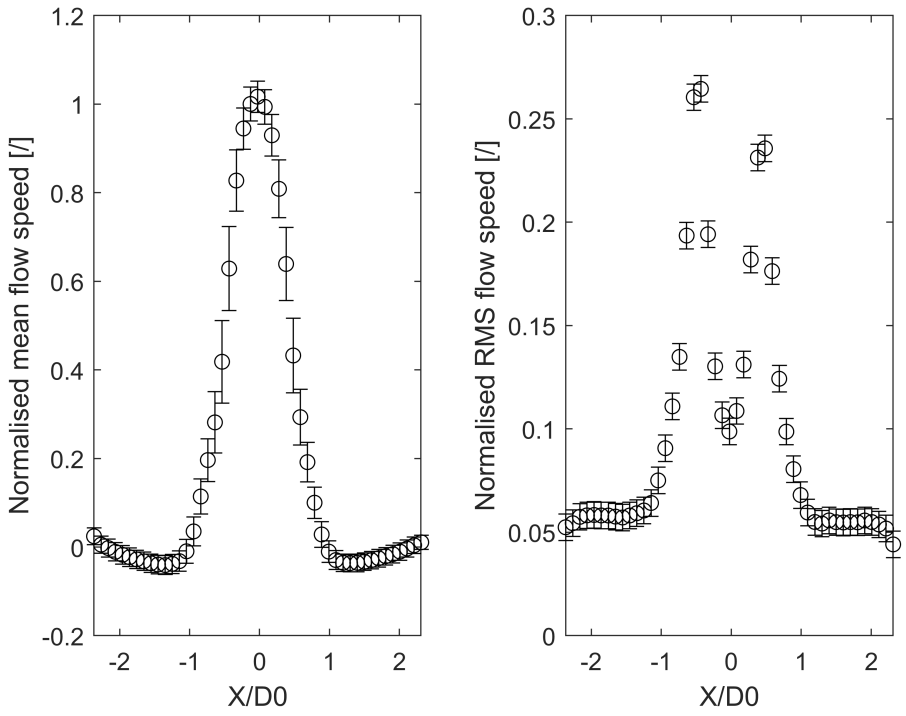

Figure 2. The mean and RMSE velocity profiles at $Y/D_0 = 0.5$ with their corresponding error bars. The errors are multiplied by 10 and only one in two data-points is shown, both for clarity of the figure.

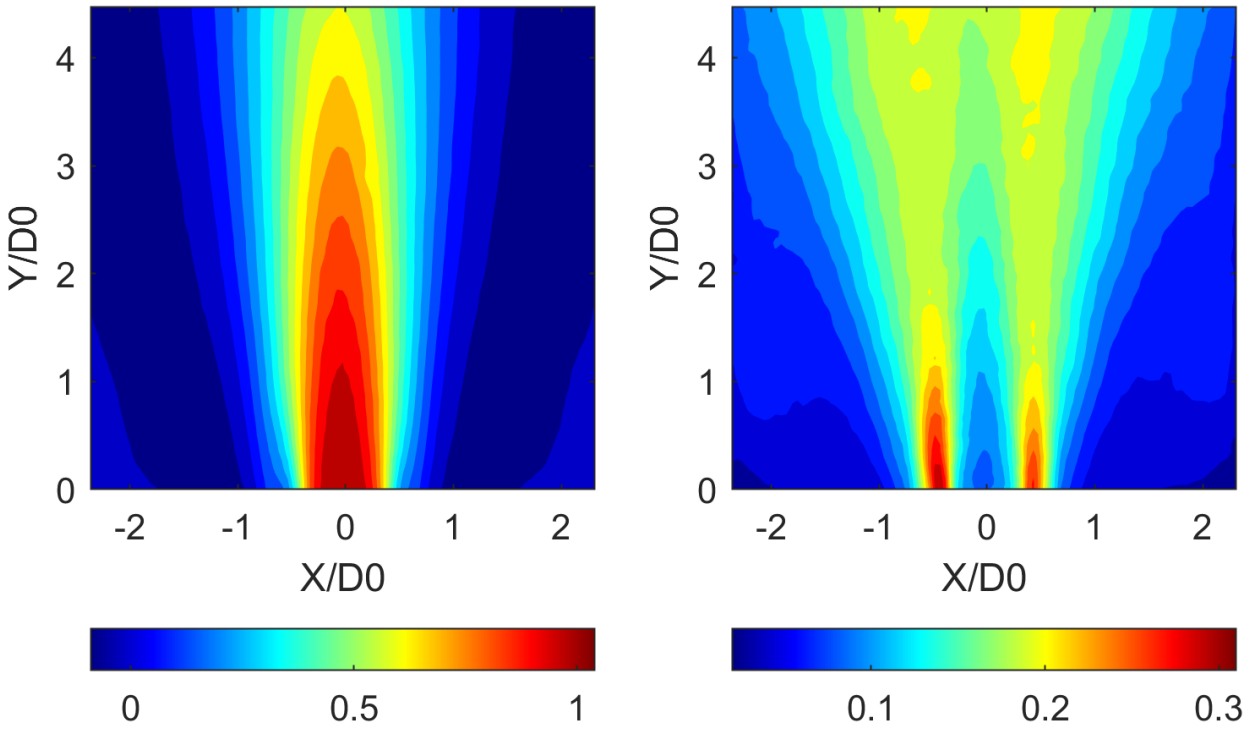

Figure 3. Left: the time-averaged axial velocity flow field and right: the RMSE of the axial velocity at Re=38400. Both are normalised with the average inlet velocity of the jet

However, the shear layer with the surroundings is influenced by the recirculation zone induced by the specific nozzle geometry (Figure 4). Further downstream the jet spreads similar to a free jet due to the large expansion ratio with a significant growth in shear layer thickness. The RMSE values shown in the right of Figure 3 also show a typical jet profile with high values in the shear layer between the jet and recirculation zone. As the jet spreads, the RMSE values decrease further downstream and the growth of the shear layer increases the width of the region with high RMSE values. Further downstream after $Y/D_0 = 3$, the values increase again due to the large scale precession of the jet, see section 3.3.

3.3. Unsteady flow field analysis

The instantaneous flow field is shown in Figure 5 at two arbitrarily time instants. Despite the axisymmetric nature of the time-averaged flow field, one can clearly see that the instantaneous flow fields are asymmetric where the jet in the left figure is deflected towards the right, while the jet

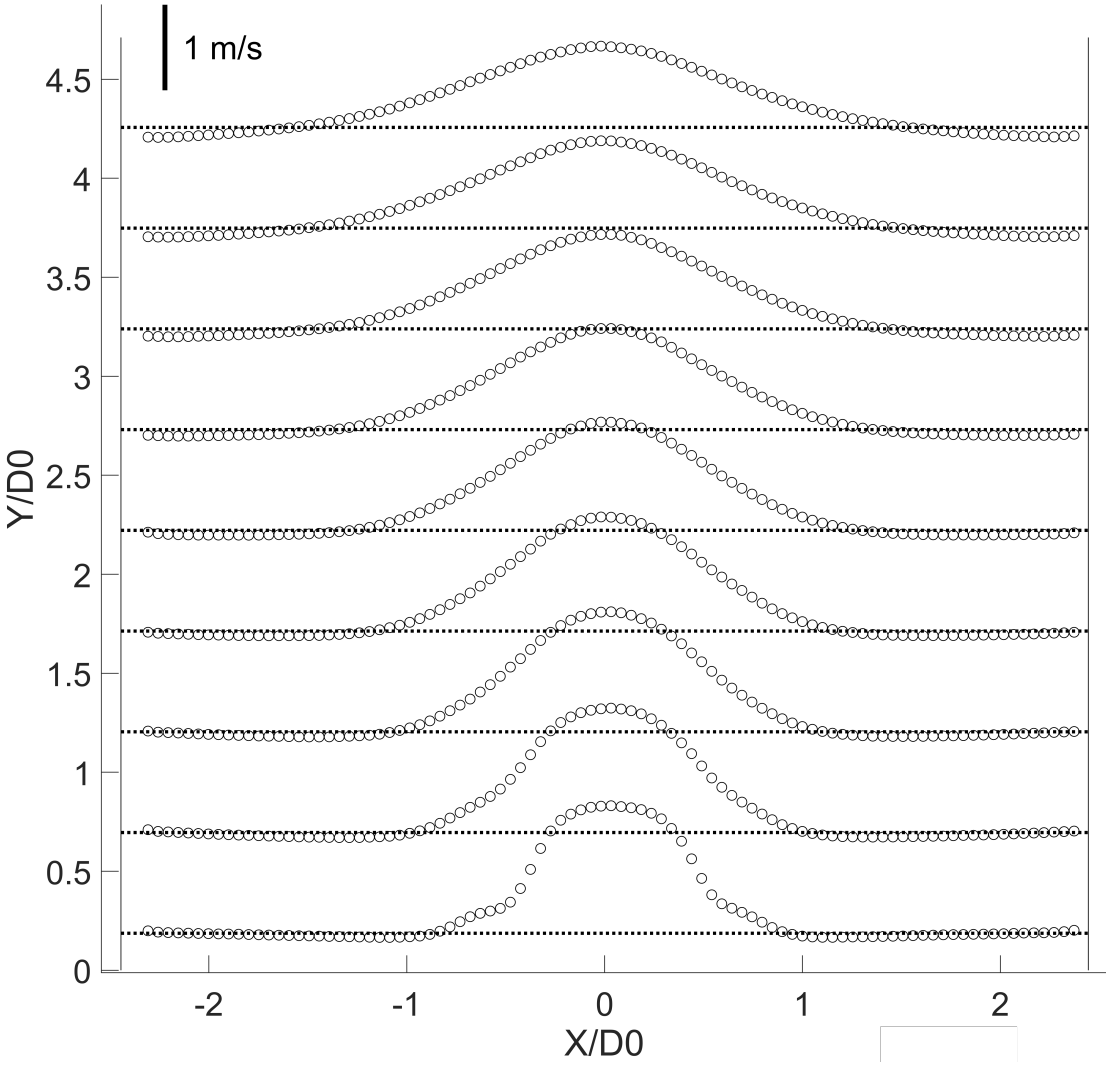

Figure 4. Time-averaged axial velocity profiles at different axial positions throughout the combustor for Re=38400

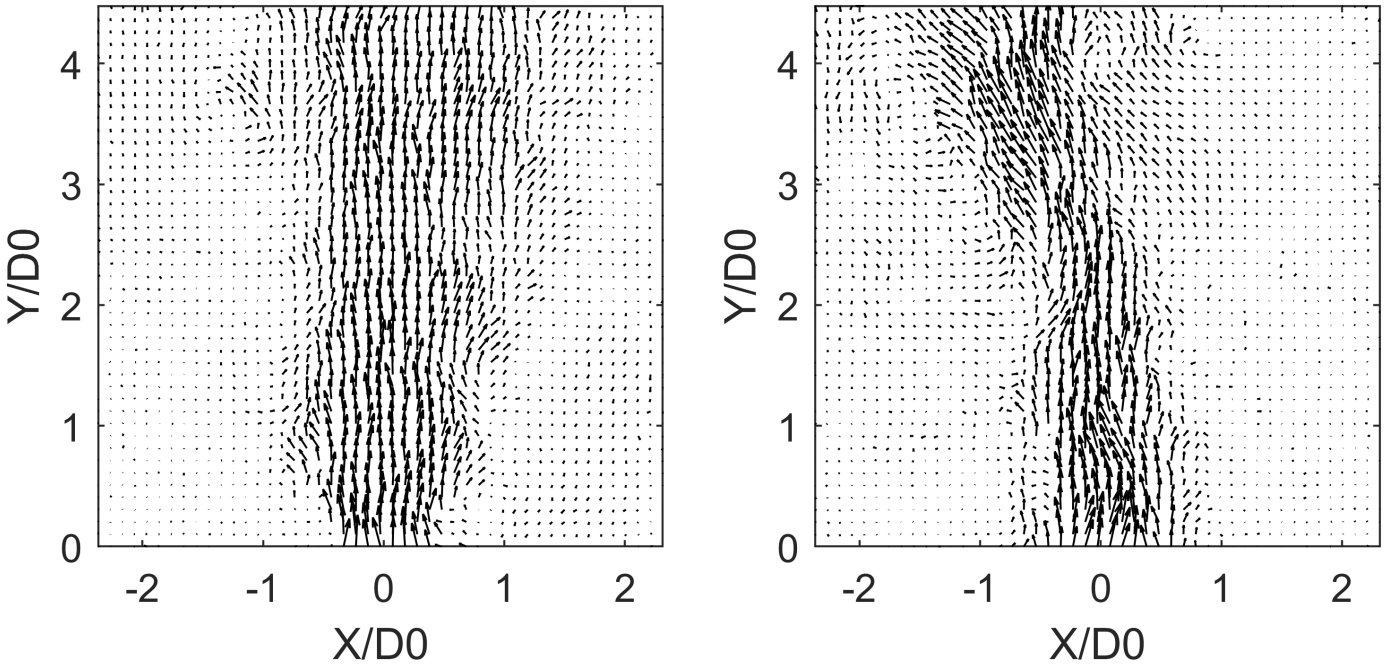

Figure 5. Instantaneous vector fields at two arbitrarily time instants

in the right figure is deflected to the left. The spatial scale of this asymmetry is much larger than the ones associated with turbulence and hence it is caused by a large scale instability in the flow field. To study the dynamics of this instability, the flow is decomposed using Spectral Proper Orthogonal Decomposition (Sieber et al., 2016). The energy content of each modepair and its corresponding Strouhal number are shown in Figure 6, for a Reynolds number of 38400. The Strouhal number is defined as, $St = \frac{fD_0}{V_y}$.The modepair with the highest energy, which is modepair 1, has an energy content of around 11% of the total turbulent kinetic energy of the flow. The harmonic correlation of the modes in a mode pair, is shown by the 'yellowness' of a dot. This high harmonic correlation can be visually represented by plotting the temporal modes of the two modes composing modepair 1, which is shown in Figure 7. This modepair has a Strouhal number of around 3×10^{-3}. A reconstruction of the velocity field using the mean field and only this specific mode pair is shown in Figure 8. The time interval between two consecutive fields is 1/4th of the temporal period of the large scale motion. Figure 8 reveals that the jet precesses around the central axis of the geometry. The out-of-plane velocity component reveals a motion in the counter-clockwise direction when viewed from the positive z-direction. The results in this study contradicts previous studies on non-swirling sudden expansion flow, as they reported no precession or large scale instabilities (Dellenback et al., 1988; Wang et al., 2004; Guo et al., 2001). The reasons for this discrepancy are most likely to be caused by overlooking these instabilities as their frequencies are very low, the higher expansion ratio or the inability of LDA, which is a point measurement technique, to capture spatial structures in the flow. With SPIV, the spatial structure of a flow field can be revealed and since to the authors' knowledge this study is the first one to apply SPOD on a non-swirling sudden expansion flow, it is also the first one to reveal the precession of the jet.

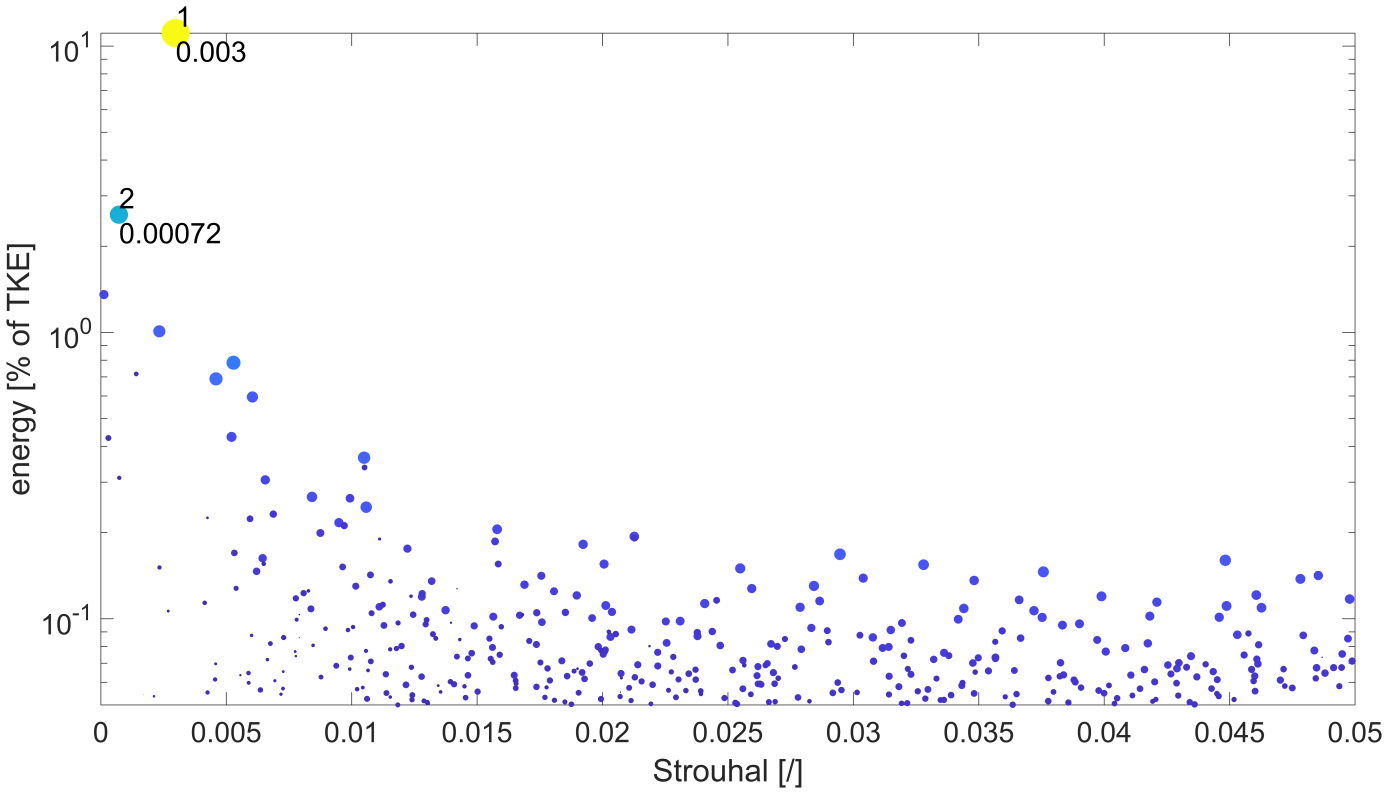

Figure 6. SPOD analysis of the flow field at Re=38400, with filter length of 102 samples

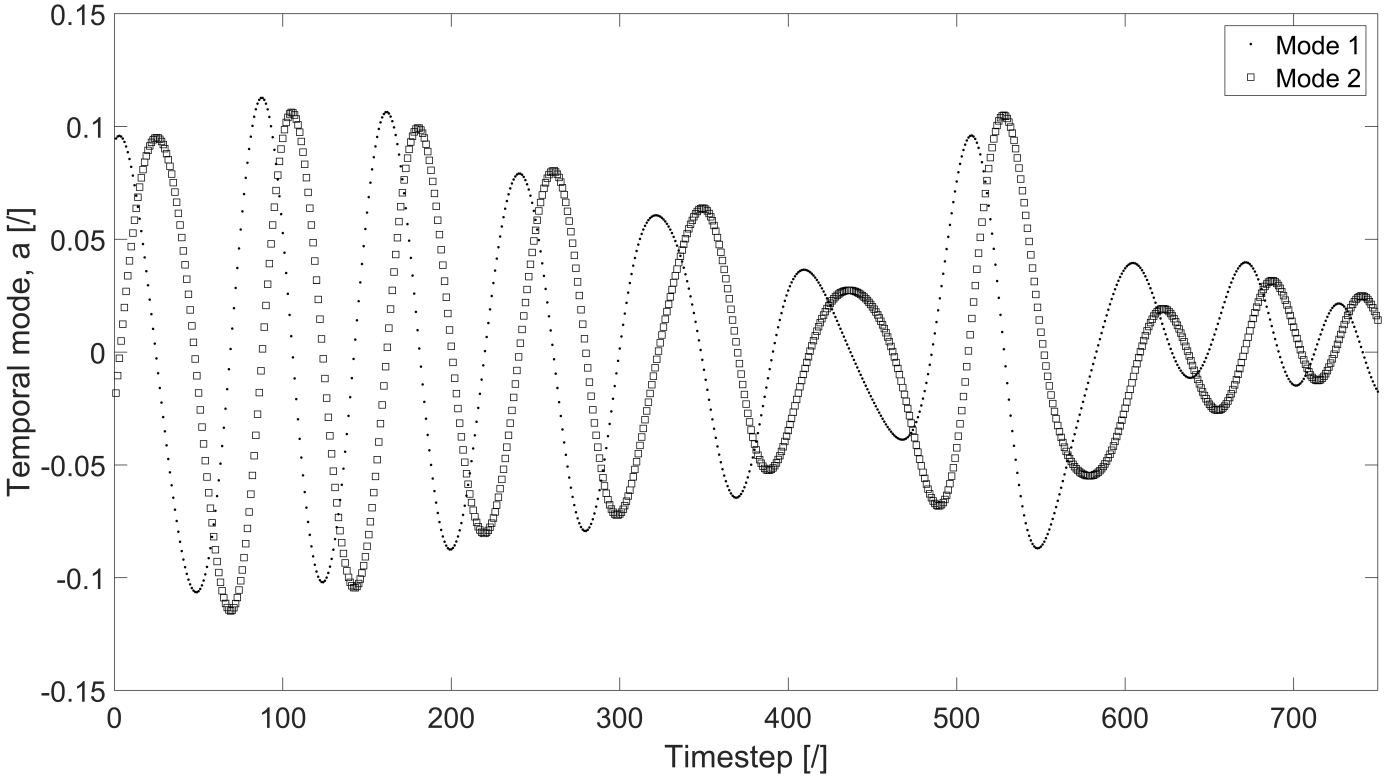

Figure 7. Temporal mode of mode 1 and 2 of modepair 1 (St=3 $\times$ 10^{-3})

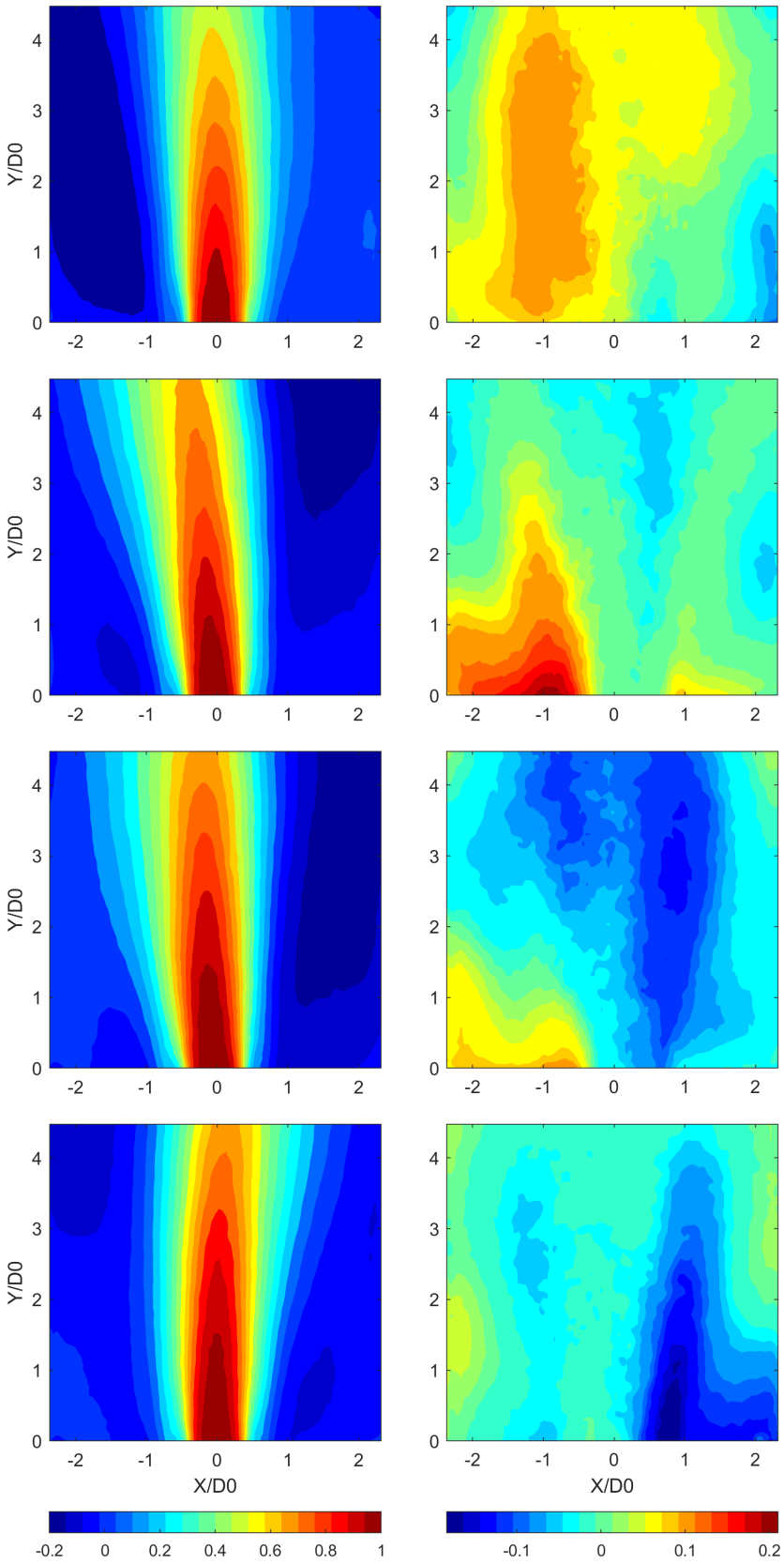

Figure 8. Reconstruction of the axial (left) and out-of-plane (right) velocity field, normalised with the mean jet velocity, using the first mode pair of the SPOD decomposition at Re=38400. Each row corresponds to a consecutive temporal snapshot with a time interval of 1/4th of the precession period between each sample

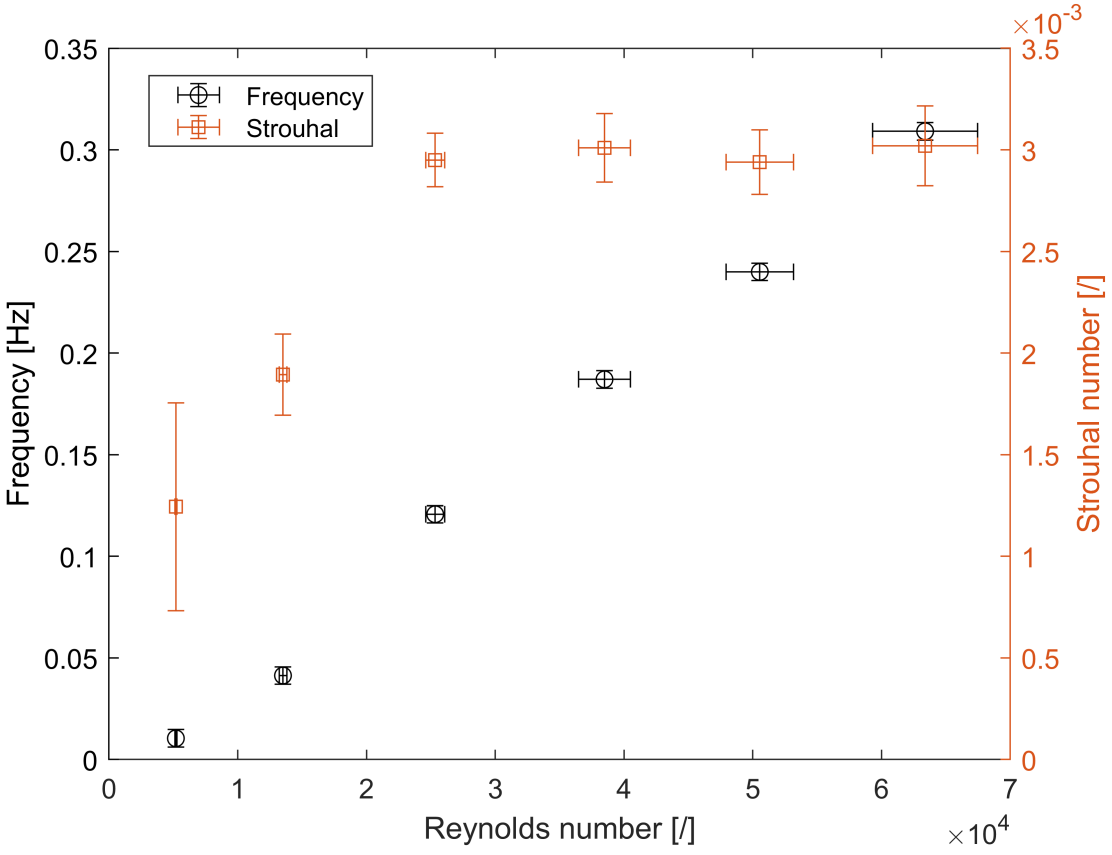

Figure 9. Strouhal number and frequency as a function of the Reynolds number.

3.4. Influence of the Reynolds number

Analysis of the flow fields at different Reynolds numbers shows that the SPOD modes of the precessing structure are very similar, showing that the large scale instability is present in the entire Reynolds number regime measured. The frequency and associated Strouhal number is shown in Figure 9. The frequency of the precession increases linearly with increasing Reynolds number. The error bar on the Strouhal number of the low Reynolds number measurements are quite big, this is due to the low frequency and the spectral resolution of the temporal decomposition. The lowest measured frequency is 0.0105Hz with a spectral resolution of 0.0043Hz, which is the measuring frequency (12.95Hz) divided by the number of samples (3000). This gives an gives an error of 41.6% for this lowest Reynolds number measurement, which is the dominant error source for the Strouhal number calculation. The Strouhal number first increases for low Reynolds numbers and then reaches a constant value of about 3×10^{-3} for higher Reynolds numbers. This Strouhal number is very close to the ones observed for annular jets, where values of 2.5×10^{-3} have been reported by Vanierschot & Van den Bulck (2011). This seems to suggest that the physical phenomena driving these instabilities are very similar for both flow topologies.

4. Conclusions

In this study, the flow field in a sudden expansion dump combustor has been studied for Reynolds numbers ranging from 5200 till 63300. Despite the axisymmetric nature of the time-averaged flow field, the instantaneous flow is asymmetric due to the presence of a large scale precession of the jet around the central axis. This precession exists in the entire Reynolds number regime measured and the frequency increases linear with increasing Reynolds number. Previous research reported that precessing structures were absent in non-swirling sudden expansion flows and could only be found in swirling sudden expansion flows. However this study shows that they are also present in non-swirling sudden expansion flows.

Acknowledgements

The funding of this research by the 'Dienst onderzoekscoördinatie (DOC) KU Leuven' through grant number C3/19/015 is gratefully acknowledged.

Nomenclature

a	Temporal Mode [/]
D_0	Inlet tube Diameter [m]
D_v	Vessel Diameter [m]
f	Frequency [Hz]
g_k	Filter coefficients Vector [/]
N	Number of samples [/]
N_f	Filter width [/]
R	Correlation Matrix [m/s]
Re	Reynolds number [/]
S	Filtered Correlation Matrix [m/s]
St	Strouhal Number [/]
Sto	Stokes Number [/]
V_y	Axial velocity [m/s]
$V(x,t)$	Velocity in space and time [m/s]
$V^\dagger(x,t)$	Fluctuating velocity in space and time [m/s]
$\overline{V}(x)$	Average velocity in space [m/s]
x	Radial position [m]
y	Axial position [m]
$Z_{\alpha/2}$	Z-score [/]
$\delta_{\overline{Ui}}$	Error on average velocity [m/s]
$\delta_{\overline{u_i u_i}}$	Error on RMSE velocity [m/s]

λ_i	Mode Energy $[m/s]$
ϕ	Spatial Mode $[m/s]$
τ_P	Response Time [s]
τ_f	Characteristic time scale of flow [s]

References

Ahmed, W. H., Ching, C. Y., & Shoukri, M. (2008). Development of two-phase flow downstream of a horizontal sudden expansion. *International Journal of Heat and Fluid Flow*, *29*(1), 194–206.

Dellenback, P. A., Metzger, D. E., & Neitzel, G. P. (1988). Measurements in turbulent swirling flow through an abrupt axisymmetric expansion. *AIAA Journal*, *26*(6), 669–681.

Durrett, R. P., Stevenson, W. H., & Thompson, H. D. (1988). Radial and axial turbulent flow measurements with an LDV in an axisymmetric sudden expansion air flow. *Journal of Fluids Engineering*, *110*(4), 367–372.

Guo, B., Langrish, T. A. G., & Fletcher, D. F. (2001). Simulation of turbulent swirl flow in an axisymmetric sudden expansion. *AIAA Journal*, *39*(1), 96–102.

Holemans, T., Yang, Z., & Vanierschot, M. (2022). Efficient reduced order modeling of large data sets obtained from cfd simulations. *Fluids*, *7*(3). Retrieved from `https://www.mdpi.com/2311-5521/7/3/110` doi: 10.3390/fluids7030110

ITTC. (2014). Guideline on the uncertainty analysis for particle image velocimetry (Computer software manual No. 7.5-01-03-03).

Raffel, M., Willert, C. E., Scarano, F., Kähler, C. J., Wereley, S. T., & Kompenhans, J. (2018). *Particle image velocimetry*. Springer International Publishing.

Rovira, M., Engvall, K., & Duwig, C. (2021). Proper orthogonal decomposition analysis of the large-scale dynamics of a round turbulent jet in counterflow. *Physical Review Fluids*, *6*(1), 014701.

Sciacchitano, A. (2019). Uncertainty quantification in particle image velocimetry. *Measurement Science and Technology*, *30*(9), 092001.

Sieber, M., Paschereit, C. O., & Oberleithner, K. (2016). Spectral proper orthogonal decomposition. *Journal of Fluid Mechanics*, *792*, 798–828.

Vanierschot, M. (2007). *Fluid mechanics and control of annular jets with and without swirl* (Doctoral dissertation, KU Leuven). Retrieved from `https://lirias.kuleuven.be/retrieve/67461`

Vanierschot, M., Müller, J. S., Sieber, M., Percin, M., van Oudheusden, B. W., & Oberleithner, K. (2020). Single- and double-helix vortex breakdown as two dominant global modes in turbulent swirling jet flow. *Journal of Fluid Mechanics*, *883*, A31.

Vanierschot, M., Percin, M., & van Oudheusden, B. W. (2021). Asymmetric vortex shedding in the wake of an abruptly expanding annular jet. *Experiments in Fluids*, *62*(4), 77. Retrieved from https://link.springer.com/10.1007/s00348-021-03177-9 doi: 10.1007/s00348-021-03177-9

Vanierschot, M., & Van den Bulck, E. (2008). The influence of swirl on the reattachment length in an abrupt axisymmetric expansion. *International Journal of Heat and Fluid Flow*, *29*(1), 75–82.

Vanierschot, M., & Van den Bulck, E. (2011). Experimental study of low precessing frequencies in the wake of a turbulent annular jet. *Experiments in Fluids*, *50 (1)*.

Wang, P., Bai, X. S., Wessman, M., & Klingmann, J. (2004). Large eddy simulation and experimental studies of a confined turbulent swirling flow. *Physics of Fluids*, *16*(9), 3306–3324.

Zhang, Y., & Vanierschot, M. (2021). Determination of single and double helical structures in a swirling jet by spectral proper orthogonal decomposition. *Physics of Fluids*, *33*(1), 015115.